Hindawi
Mathematical Problems in Engineering
Volume 2020, Article ID 9026804, 15 pages
https://doi.org/10.1155/2020/9026804

Research Article

On the Nonlinear Seismic Responses of Shock Absorber-Equipped Porcelain Electrical Components

Zhubing Zhu,[1,2,3] Lingxin Zhang,[1,2] Yongfeng Cheng,[3] Hulun Guo,[4] and Zhicheng Lu[3]

[1]*Institute of Engineering Mechanics, China Earthquake Administration, Harbin 150080, China*
[2]*Key Laboratory of Earthquake Engineering and Engineering Vibration, China Earthquake Administration, Harbin 150080, China*
[3]*China Electric Power Research Institute, Beijing 100192, China*
[4]*Department of Mechanics, Tianjin University, Tianjin 300072, China*

Correspondence should be addressed to Lingxin Zhang; lingxin_zh@126.com

Received 2 February 2020; Accepted 29 February 2020; Published 15 May 2020

Guest Editor: Ping Zhao

Porcelain electrical equipment is prone to brittle failure due to resonance under seismic effects. To improve its seismic resistance, some researchers have conducted research on shock absorption technology for porcelain electrical equipment. However, extant research fails to provide a detailed and systematic study of the effect of the nonlinear characteristics of these shock absorbers on the performance of equipment under seismic effects. This paper provides a theoretical analysis, verified by shaking table testing, of the performance of a 1000 kV pillar-type porcelain lightning arrester. The Bouc–Wen model is fitted to the force-displacement curve of hysteretic nonlinear metal shock absorbers, and a dynamic model of, and equations for, pillar-type porcelain electrical components are derived, taking into account their nonlinear characteristics. This reveals the influence of the nonlinear characteristics of shock absorbers on the nonlinear seismic response characteristics of these components. Our results indicate that the seismic responses of pillar-type porcelain components can be effectively suppressed by hysteretic nonlinear shock absorbers and that the greater the intensity of the seismic waves, the more obvious the efficiency of shock absorption. However, as the installation radius and yield force of the installed shock absorbers increase, their shock absorption efficiency gradually decreases.

1. Introduction

As voltage classes have improved and the volume and mass of substation electrical equipment have been optimised, the increasing complexity of its structural systems has been paralleled by increases in its "height, size, flexibility, and weight" characteristics, exacerbating its seismic vulnerability and increasing risks of damage during earthquakes [1]. The natural frequency of pillar-type porcelain electrical components, especially ultra-high-voltage electrical equipment, is relatively low, mostly ranging from 1 to 2 Hz [2]. As this falls within the predominant frequency range of seismic waves, such equipment is vulnerable to large seismic forces. In addition, such equipment is made of brittle porcelain material, with poor energy dissipation capability, making it susceptible to severe damage under seismic loading [3–6]. Previous earthquake events have revealed that pillar-type porcelain electrical equipment is prone to brittle failure due to resonance under seismic loading [7–11]. Predominant failure modes include bushing root fracture and equipment dislocation at flange joints due to flange cement failure. An additional mode of earthquake damage reflects tensile stresses affecting interconnecting cables [12–15]. Figure 1 depicts typical seismic loading-induced equipment damage: the upper component is a porcelain insulator and the lower one is a frame. Engineering applications generally use lattice and cylindrical steel frames, or cylindrical concrete frames, with lattice steel frames generally adopted for equipment of voltage classes in excess of 500 kV. In addition, pillar-type porcelain insulators are sometimes directly mounted on a firewall or foundation, without a supporting frame.

Figure 1: Seismic damage to pillar-type porcelain insulators.

Research on shock absorption technology to improve the seismic capacity of pillar-type porcelain insulators has been carried out in China and abroad [16]. China Electric Power Research Institute Co., Ltd. developed a shear-type shock absorber for electrical equipment, which is shown in Figure 2. These are designed to be installed between insulator equipment and their frame, via connecting bolt holes on the flange at the bottom of each equipment. Under normal conditions, these devices act as bolts connecting the insulators with their frames. For equipment that does not need frame in actual engineering, shock absorbers are installed between firewall and foundation. Under seismic loading, each shock absorber's jacket moves up and down relative to its central shaft, and an internal lead alloy element undergoes shear deformation, dissipating seismic energy to achieve shock absorption. Siemens has developed a viscoelastic damper for installation between electrical equipment frames and foundations, as shown in Figure 3. During earthquakes, this damper's piston rod is displaced within it, displacing hydraulic oil for a damping effect. Toshiba has developed a centripetal shock absorber suitable for pillar components, as shown in Figure 4. This device is installed between the electrical equipment and its frame, dissipating earthquake energy via compressive deformation of internal discs. The inner part of the centripetal shock absorber is vertically arranged and combined by discs, which can only be pressed and cannot be pulled. Therefore, the device needs to be installed in two layers; two centripetal shock absorbers in the upper layer and the lower layer at the same position are connected in series via a bolt bar to ensure the shock absorber can consume earthquake energy in tension and compression state.

To date, numerous scholars have undertaken research into the seismic properties of pillar-type porcelain insulators and nonlinear theoretical analysis of related shock absorber-equipped structural systems. Cheng Yongfeng et al. studied the nonlinear responses of shock absorber-equipped pillar-type porcelain insulators under harmonic excitation [17]. Cheng Yongfeng et al. studied the seismic performance of 1000 kV lightning arresters and transformers connected by rigid tubular busbar through shaking table testing [18]. Ye Lieping et al. proposed a nonlinear seismic analysis model for concrete structure, capable of accurately simulating their nonlinear responses to seismic effects [19]. Jean-Bemard

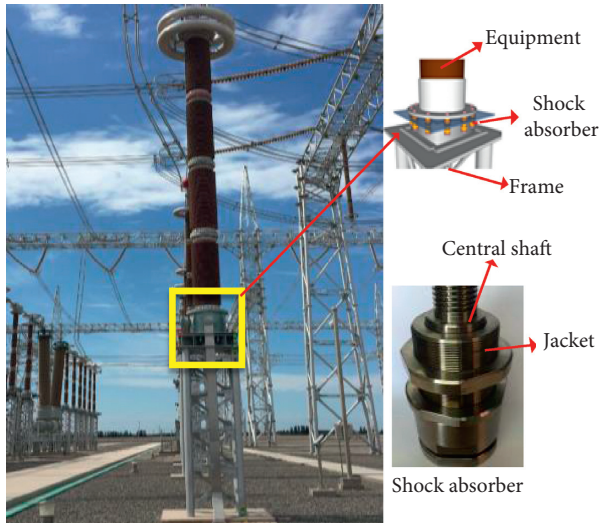

Figure 2: China Electric Power Research Institute's shear-type shock absorber and installation details.

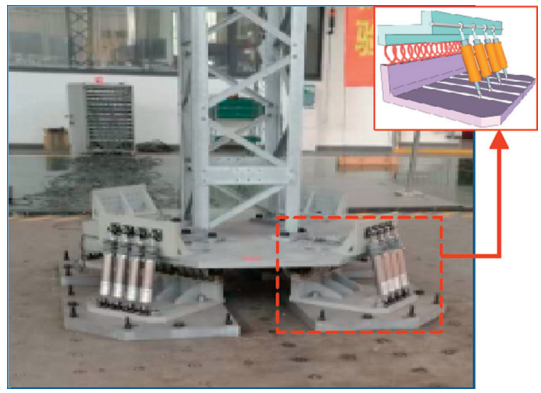

Figure 3: Siemens' viscoelastic damper and installation details.

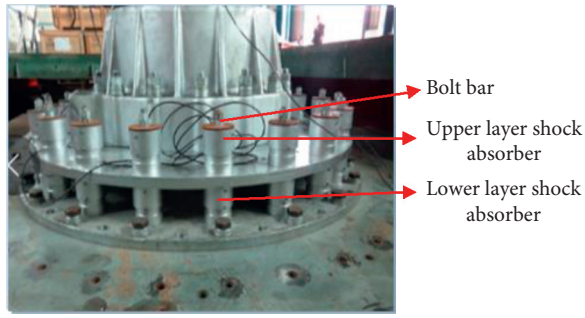

Figure 4: Toshiba's (Japan) centripetal shock absorber and installation details.

Dastous et al. conducted both static and dynamic tests of fixture wiring in order to assess its influence on the seismic performance of electrical equipment. They determined that wiring forms a nonlinear system during earthquakes and that designs retaining a certain degree of relaxation in wiring proved helpful in reducing the nonlinear coupling of interconnected equipment [20–22]. Robyn et al. used

nonlinear frictional contact elements to simulate shock absorbers and performed nonlinear time history analysis on structures equipped with these damping devices. Through comparison of multiple schemes, the accuracy of their analysis was verified, providing a basis for the development of nonlinear shock absorber designs [23].

Under seismic loading of shock absorber-equipped pillar-type porcelain insulator component systems, the shock absorbers are the components with most obvious nonlinear characteristics. These dissipate seismic energy in a nonlinear fashion to reduce the insulators' seismic response. However, while scholars have carried out research on the seismic performance of pillar-type porcelain insulators, as yet this fails to provide a detailed, systematic study of the effects of shock absorbers' nonlinear characteristics on the performance of porcelain insulators under seismic effects. And when pillar-type porcelain electrical components are equipped with shock absorbers with nonlinear characteristics, the structural system as a whole becomes more complex. The application of nonlinear theory to the seismic analysis of these structural systems can thus make a contribution toward raising the level of seismic analysis and of seismic design theory.

2. Dynamic Model and Equations

For this paper, nonlinear dynamic modeling of a 1000 kV pillar-type porcelain lightning arrester with shear-type shock absorbers without frames was conducted, and its dynamic equations were solved, in order to analyze the nonlinear seismic responses of the pillar-type porcelain components. Figure 5 provides a schematic diagram of these lightning arresters. They are composed of four pillar-type porcelain elements connected by flanges. These elements are numbered 1–4 from top to bottom. The main structural parameters of the equipment are shown in Table 1, where the elastic modulus of their porcelain material is 1.1×10^{11} N/m^2 and the weights of the top equalizing ring and other accessories (joints with electrodes and components) are 290 kg and 1801 kg, respectively. According to the shock-absorption design scheme, 20 shear-type shock absorbers are installed at the bottom of the lightning arrester.

2.1. Mechanical and Dynamic Model of the Shock Absorber. The dimensions of the lead alloy in the shock absorber are selected according to the expected seismic intensity, the required damping efficiency, and the number of bolt holes available for installation of these devices. The "restoring force-displacement" test curve of the single shock absorber used in this paper is shown in Figure 6. This figure shows obvious hysteretic nonlinearity. Shock absorber's design parameters are as follows: the yield force is 20 kN, the rigidity before yield is 80 kN/mm, and the equivalent damping ratio is 35%. The commonly used nonlinear models are elastic-plastic mechanical model, viscoelastic mechanical model, and viscous restoring force model. Whether it is an elastic-plastic mechanical model or a viscoelastic mechanical model, there is a sudden change of stiffness at the model's four corners, which is not consistent with the actual situation. Therefore, a smooth curve should be adopted to fit the restoring force-displacement curve of the damping device. The Bouc–Wen model, one of the viscous restoring force models, which has been widely adopted in engineering, can be well fit to this type of nonlinear hysteretic curve and was therefore used to model the shock absorber.

A typical Bouc–Wen model can be described by the following equations:

$$\begin{aligned} F &= k_L \xi + k_N Z, \\ \dot{Z} &= \left[\lambda - (\gamma \operatorname{sign}(\dot{\xi} Z) + \beta)|Z|^n\right]\dot{\xi}, \end{aligned} \tag{1}$$

where F represents the elastic force, ξ represents the displacement, $\dot{\xi}$ represents the displacement velocity, and γ is a parameter related to the yield force of the model.

The parameters of the Bouc–Wen model were determined by comparison of results from the theoretical model and from testing. Figure 7 shows a comparison between the Bouc–Wen model estimates and test results for the shock absorber's force-displacement curve. The Bouc–Wen model uses the following parameters: $k_L = 1 \times 10^6$ N/m, $k_N = 120 \times 10^6$ N/m, $\lambda = 1$, $\gamma = 5000$, $\beta = 1$, and $n = 1$.

In Figure 7, the black lines indicate the test results and the colored line represents estimates derived using the calibrated Bouc–Wen model. The two are in good agreement. In addition, the upper half of the Bouc–Wen model's curve is the result when $\dot{\theta} > 0$, while the lower half is the result when $\dot{\theta} < 0$l; ξ is a function of θ.

We assume that N shock absorbers are uniformly distributed at the bottom of the porcelain pillar, each separated from the next by an angle of $2\pi/N$, as shown in Figure 8(a). A mechanical model of the shock absorber joints is shown in Figure 8(b).

The connection between the shock absorber and the cement part of the flange at the base of the equipment is equivalent to a series spring [17]. The angle of the shock absorbers' surface of action is φ_1, and the spring angle relative to the cement part of the flange at the base of the equipment is φ_2. The angle of the first porcelain pillar is thus $\theta_1 = \varphi_1 + \varphi_2$.

The elastic force experienced by the shock absorber can be written as follows:

$$F_i = k_L \xi_i + k_N Z_i, \tag{2}$$

where $i = 1, 2, 3, \ldots, N$. This system is also governed by several other equations as follows:

$$\begin{aligned} \dot{Z}_i &= \left[\lambda - \left(\gamma \operatorname{sign}\left(Z_i \dot{\xi}_i\right) + \beta\right)\left|Z_i\right|^n\right]\dot{\xi}_i, \\ \xi_i &= \xi_0 + \varphi_1 R \sin \alpha_i, \end{aligned} \tag{3}$$

where ξ_0 is the static deformation and $\alpha_i = (i-1)\ 2\pi/N$. Denoting the spring stiffness of the flange at the bottom of the first porcelain pillar as k_1, this can be expressed as follows:

$$k_1 \varphi_2 = \sum_{i=1}^{N} F_i R \sin \alpha_i = K \theta_1, \tag{4}$$

where K is the equivalent stiffness. By combining $\theta_1 = \varphi_1 + \varphi_2$ with equation (4), the following equation can be derived:

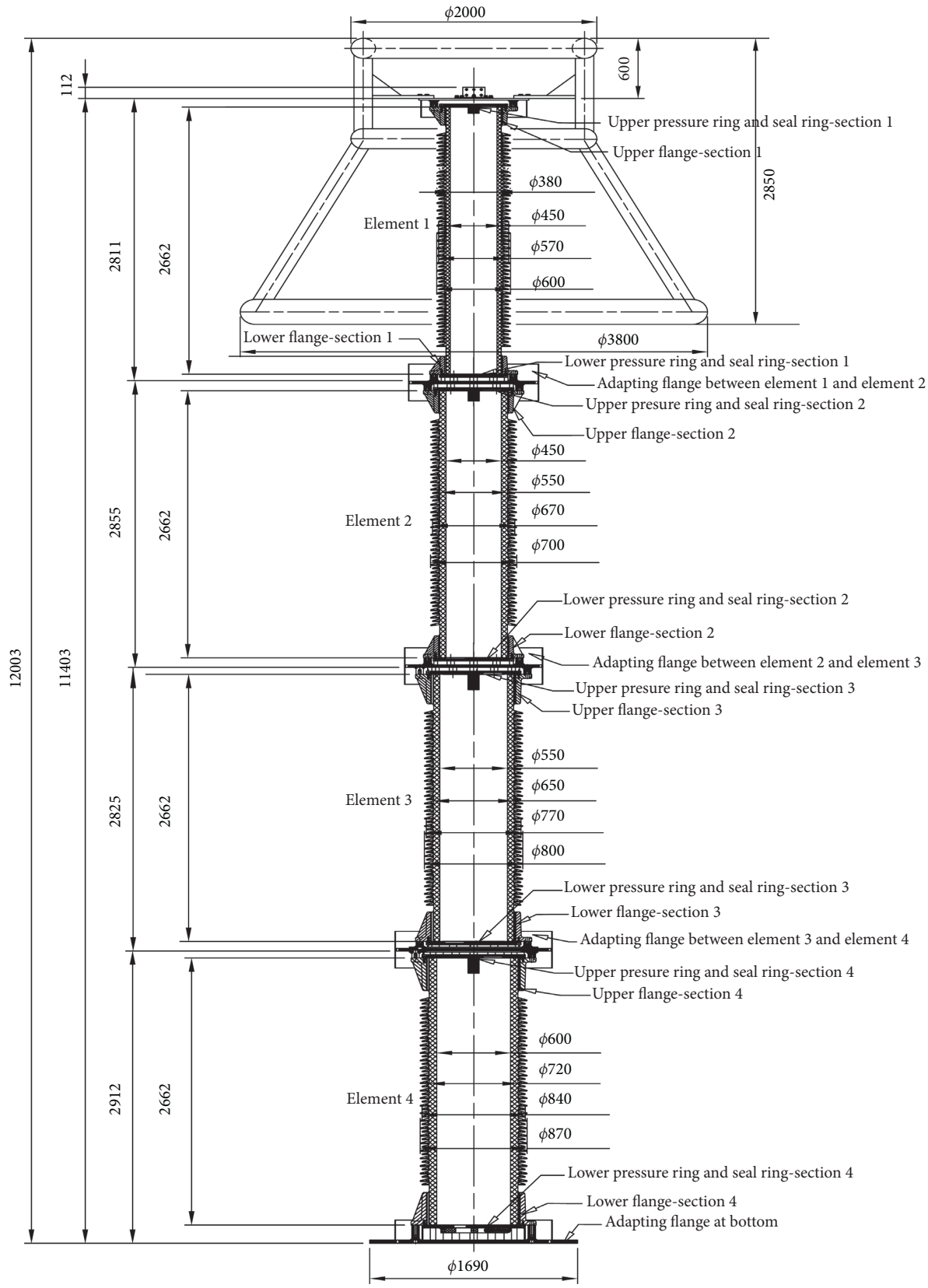

Figure 5: Schematic diagram of lightning arrester.

Table 1: Lightning arrester structural parameters.

Element no.	1	2	3	4
Weight (kg)	940	1212	1349	1571
Length (m)	2.662	2.662	2.662	2.662
Inner diameter (m)	0.38	0.45	0.55	0.60
Outer diameter (m)	0.45	0.55	0.65	0.72

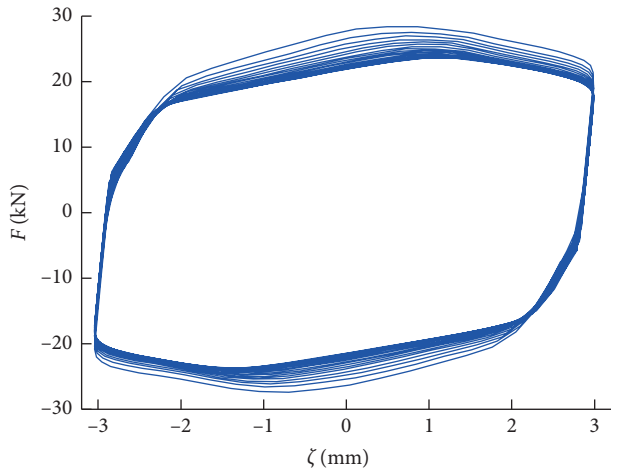

Figure 6: "Restoring force-displacement" curve of shock absorber.

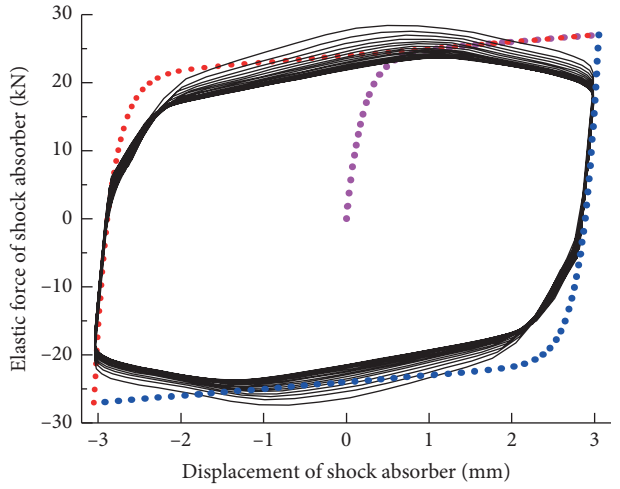

Figure 7: Shock absorber force-displacement curve: Bouc–Wen model estimates and test results.

$$\theta_1 = d_1\varphi_1 + d_2\sum_{i=1}^{N} Z_i \sin\alpha_i, \tag{5}$$

where $d_1 = 1 + (k_L R^2/k_1)\sum_{i=1}^{N}\sin^2\alpha_i$ and $d_2 = k_N R/k_1$.

2.2. Calculation of Flange Joint Bending Stiffness. The pillar-type porcelain components are connected by flanges, with one flange at the upper and lower end of each section. Stiffness is generated at both the cement flanges and porcelain bushings, as shown in Figure 9.

The upper and lower flanges generate total stiffness equivalent to the stiffness of two springs in series. If the stiffness of the flange at the bottom of the upper porcelain pillar is denoted by k_{id}, and the stiffness of the flange at the top of the lower porcelain pillar is denoted by $k_{(i-1)u}$, the equivalent stiffness, k_i, of the two sections of the porcelain pillar can be expressed as follows:

$$k_i = \frac{k_{\mathrm{id}}k_{(i-1)u}}{k_{\mathrm{id}} + k_{(i-1)u}}. \tag{6}$$

The bending stiffness of upper and lower flanges can be calculated according to the equation specified in the *Technical Specification for Seismic Design of Ultra-High-Voltage Porcelain Insulating Electrical Equipment and Installation/Maintenance of Energy Dissipation Devices* (Q/GDW 11132-2013) published by the China Electric Power Research Institute [24]:

$$k_{\mathrm{id}} = \frac{\beta_d d_d h_d^2}{t_d},$$
$$k_{\mathrm{iu}} = \frac{\beta_u d_u h_u^2}{t_u}, \tag{7}$$

where d_u and d_d are the outer diameters of the cement elements between the porcelain bushing and the upper and lower flanges, respectively; h_u and h_d are the heights of the cement between the porcelain bushing and the upper and lower flanges, respectively; t_u and t_d are the clearance distances between the porcelain bushings and the upper and lower flanges, respectively; and β_u and β_d are the bending stiffness coefficients at the connections between the porcelain bushing and the upper and lower flanges, respectively, the value of which is 6.54×10^7 when the outer diameter of the porcelain bushing at the cement element is smaller than 275 mm and is 5.0×10^7 when the outer diameter of the porcelain bushing at the cement element is larger than 275 mm, derived by linear interpolation when the outer diameter of the porcelain bushing at the cement element lies between 275 and 375 mm.

2.3. Dynamic Equation of Shock Absorber and Pillar-Type Porcelain Component System. Taking the 1000 kV pillar-type porcelain lightning arrester as an example, the flange at the bottom of the first pillar-type porcelain component is connected in series with the shock absorber and then consolidated. The elastic potential energy of the shock absorber and the flange joint at the bottom of the first porcelain pillar can now be written as follows:

$$U_A = \frac{1}{2}K\theta_1^2. \tag{8}$$

Differentiating this is equivalent to the following:

$$\delta U_A = K\theta_1\delta\theta_1. \tag{9}$$

If there are N_c porcelain pillar components, there will also be N_c flange joints, and the total elastic potential energy at these flange joints can be calculated as follows:

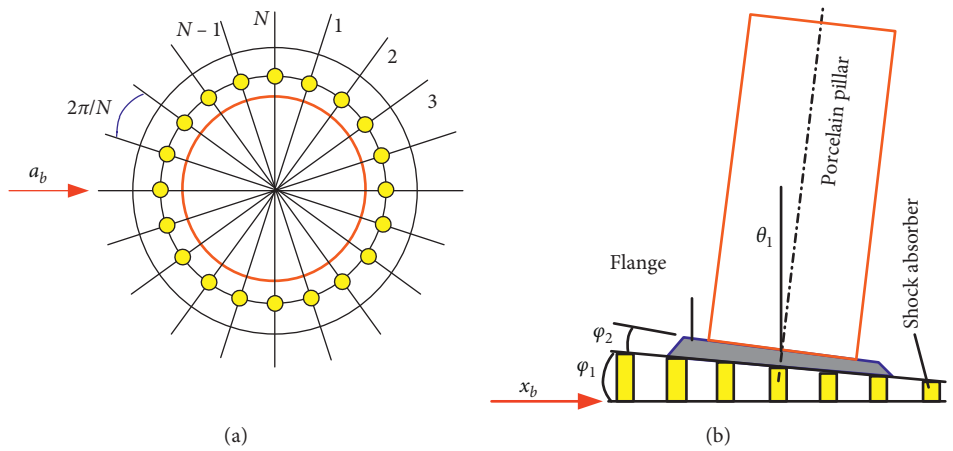

Figure 8: (a) Distribution of shock absorbers at the base of porcelain pillar. (b) Mechanical model of shock absorber joints.

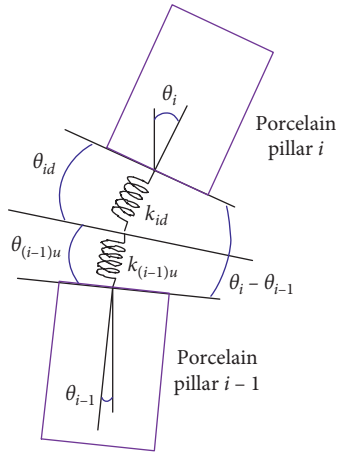

Figure 9: Flange joint.

$$U_k = \frac{1}{2}k_1\theta_1^2 + \sum_{i=2}^{N_c}\left[\frac{1}{2}k_i(\theta_i - \theta_{i-1})^2\right]. \tag{10}$$

The rotation of the porcelain pillars also causes changes in their gravitational potential energy, and their total gravitational potential energy is as follows:

$$U_g = -\frac{1}{2}\sum_{i=1}^{Nc} m_i g\left(\sum_{j=1}^{i} L_j\theta_j^2 - \frac{1}{2}L_i\theta_i^2\right), \tag{11}$$

where L_i and L_j are the lengths of the i^{th} and j^{th} porcelain pillars, respectively.

The total potential energy of the system comprising the porcelain pillars and shock absorbers can be calculated as follows:

$$U = U_k + U_g + U_A. \tag{12}$$

Figure 10 is a schematic diagram of the velocity relationships for the i^{th} porcelain pillar. The dynamic energy of the porcelain pillar includes translational and rotational dynamic energy, described by the following equation:

$$T = \frac{1}{2}\sum_{i=1}^{N_c} m_i v_{c,i}^2 + \frac{1}{2}\sum_{i=1}^{N_c}\frac{1}{12}m_i L_i^2\dot{\theta}_i^2, \tag{13}$$

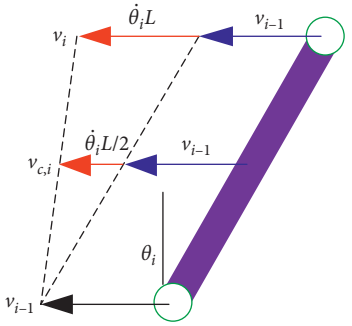

Figure 10: Velocity relationships of the i^{th} porcelain pillar.

where $v_{c,i}$ is the velocity of the centroid of the i^{th} porcelain pillar.

Figure 10 depicts the dynamics of a porcelain pillar, again taking a 1000 kV pillar-type porcelain lightning arrester as an example. The velocity of the flange at the bottom of the first porcelain pillar can be expressed as follows:

$$v_0 = \dot{x}_b, \tag{14}$$

where x_b is seismic effect-induced ground displacement.

The velocity of the centroid of the first porcelain pillar can then be calculated as follows:

$$v_{c,1} = v_0 + \frac{1}{2}L_1\dot{\theta}_1. \tag{15}$$

The velocity of the second porcelain pillar's centroid is then

$$v_{c,2} = v_0 + L_1\dot{\theta}_1 + \frac{1}{2}L_2\dot{\theta}_2. \tag{16}$$

The velocity of the third porcelain pillar's centroid can be written as

$$v_{c,3} = v_0 + L_1\dot{\theta}_1 + L_2\dot{\theta}_2 + \frac{1}{2}L_3\dot{\theta}_3. \tag{17}$$

And the velocity of the fourth porcelain pillar's centroid can be expressed as

$$v_{c,4} = v_0 + L_1\dot{\theta}_1 + L_2\dot{\theta}_2 + L_3\dot{\theta}_3 + \frac{1}{2}L_4\dot{\theta}_4. \tag{18}$$

The system's nonlinear dynamic equation can be derived using Hamilton's principle. Variation in the system's kinetic energy can be expressed as follows:

$$\delta T = -\sum_{i=1}^{N_c}\begin{bmatrix} m_i\left(\ddot{x}_b + \sum_{j=1}^{i} L_j\ddot{\theta}_j - \frac{1}{2}L_i\ddot{\theta}_i\right)\delta\left(\sum_{j=1}^{i} L_j\theta_j - \frac{1}{2}L_i\theta_i\right) + \\ \\ \frac{1}{12}m_iL_i^2\ddot{\theta}_i\delta\theta_i \end{bmatrix}. \tag{19}$$

The change in its potential energy can be written as

$$\delta U = k_1\theta_1\delta\theta_1 - \sum_{i=1}^{Nc} m_ig\left(\sum_{j=1}^{i} L_j\theta_j\delta\theta_j - \frac{1}{2}L_i\theta_i\delta\theta_i\right) + \sum_{i=2}^{Nc}\left[k_i\left(\theta_i - \theta_{i-1}\right)\right]\delta\left(\theta_i - \theta_{i-1}\right). \tag{20}$$

The dynamic and potential energy of the system can now be substituted into Hamilton's variational equation:

$$\int_{t_1}^{t_2}(\delta T - \delta U)\mathrm{d}t = 0. \tag{21}$$

This yields the following dynamic equation for the system:

$$\begin{aligned}
&\left(\frac{1}{3}m_1 + \sum_{i=2}^{4} m_i\right)L_1^2\ddot{\theta}_1 + \left(\frac{1}{2}m_2 + \sum_{i=3}^{4} m_i\right)L_1L_2\ddot{\theta}_2 + \left(\frac{1}{2}m_3 + m_4\right)L_1L_3\ddot{\theta}_3 \\
&\quad + \frac{1}{2}m_4L_1L_4\ddot{\theta}_4 + k_1\theta_1 - k_2\left(\theta_2 - \theta_1\right) - \left(\frac{1}{2}m_1 + \sum_{i=2}^{4} m_i\right)gL_1\theta_1 \\
&= -\left(\frac{1}{2}m_1 + \sum_{i=2}^{4} m_i\right)L_1\ddot{x}_b, \\
&\quad \cdot \left(\frac{1}{2}m_2 + \sum_{i=3}^{4} m_i\right)L_1L_2\ddot{\theta}_1 + \left(\frac{1}{3}m_2 + \sum_{i=3}^{4} m_i\right)L_2^2\ddot{\theta}_2 + \left(\frac{1}{2}m_3 + m_4\right)L_2L_3\ddot{\theta}_3 \\
&\quad + \frac{1}{2}m_4L_2L_4\ddot{\theta}_4 + k_2\left(\theta_2 - \theta_1\right) - k_3\left(\theta_3 - \theta_2\right) - \left(\frac{1}{2}m_2 + \sum_{i=3}^{4} m_i\right)gL_2\theta_2 \\
&= -\left(\frac{1}{2}m_2 + \sum_{i=3}^{4} m_i\right)L_2\ddot{x}_b, \\
&\quad \cdot \left(\frac{1}{2}m_3 + m_4\right)L_1L_3\ddot{\theta}_1 + \left(\frac{1}{2}m_3 + m_4\right)L_2L_3\ddot{\theta}_2 + \left(\frac{1}{3}m_3 + m_4\right)L_3^2\ddot{\theta}_3 \\
&\quad + \frac{1}{2}m_4L_3L_4\ddot{\theta}_4 + k_3\left(\theta_3 - \theta_2\right) - k_4\left(\theta_4 - \theta_3\right) - \left(\frac{1}{2}m_3 + m_4\right)gL_3\theta_3 \\
&= -\left(\frac{1}{2}m_3 + m_4\right)L_3\ddot{x}_b, \\
&\quad \frac{1}{2}m_4\left(L_1L_4\ddot{\theta}_1 + L_2L_4\ddot{\theta}_2 + L_3L_4\ddot{\theta}_3\right) + \frac{1}{3}m_4L_4^2\ddot{\theta}_4 + k_4\left(\theta_4 - \theta_3\right) \\
&\quad - \frac{1}{2}m_4gL_4\theta_4 = -\frac{1}{2}m_4L_4\ddot{x}_b.
\end{aligned} \tag{22}$$

This equation can be rewritten in the matrix form as

$$\mathbf{M}\ddot{\theta} + \mathbf{K}\boldsymbol{\theta} + \mathbf{N}(\boldsymbol{\theta}) = \mathbf{F}\ddot{x}_b, \tag{23}$$

where

$$M = \begin{bmatrix} M_{11} & M_{12} & M_{13} & M_{14} \\ M_{21} & M_{22} & M_{23} & M_{24} \\ M_{31} & M_{32} & M_{33} & M_{34} \\ M_{41} & M_{42} & M_{43} & M_{44} \end{bmatrix},$$

$$K = \begin{bmatrix} K_{11} & -k_2 & 0 & 0 \\ -k_2 & K_{22} & -k_3 & 0 \\ 0 & -k_3 & K_{33} & -k_4 \\ 0 & 0 & -k_4 & K_{44} \end{bmatrix},$$

$$N(\theta) = \begin{Bmatrix} -k_1\varphi_1 \\ 0 \\ 0 \\ 0 \end{Bmatrix}, \tag{24}$$

$$F = -f \begin{Bmatrix} \left(\frac{1}{2}m_1 + \sum_{i=2}^{4} m_i\right)L_1 \\ \left(\frac{1}{2}m_2 + \sum_{i=3}^{4} m_i\right)L_2 \\ \left(\frac{1}{2}m_3 + m_4\right)L_3 \\ \frac{1}{2}m_4 L_4 \end{Bmatrix}.$$

Several other equations complete the system as follows:

$$\theta = \{\theta_1 \ \ \theta_2 \ \ \theta_3 \ \ \theta_4\}^T,$$

$$M_{11} = \left(\frac{1}{3}m_1 + \sum_{i=2}^{4} m_i\right)L_1^2,$$

$$M_{12} = M_{21} = \left(\frac{1}{2}m_2 + \sum_{i=3}^{4} m_i\right)L_1L_2,$$

$$M_{13} = M_{31} = \left(\frac{1}{2}m_3 + m_4\right)L_1L_3,$$

$$M_{14} = M_{41} = \frac{1}{2}m_4L_1L_4,$$

$$M_{22} = \left(\frac{1}{3}m_2 + \sum_{i=3}^{4} m_i\right)L_2^2,$$

$$M_{23} = M_{32} = \left(\frac{1}{2}m_3 + m_4\right)L_2L_3,$$

$$M_{24} = M_{42} = \frac{1}{2}m_4L_2L_4, \tag{25}$$

$$M_{33} = \left(\frac{1}{3}m_3 + m_4\right)L_3^2,$$

$$M_{34} = M_{43} = \frac{1}{2}m_4L_3L_4,$$

$$M_{44} = \frac{1}{3}m_4L_4^2,$$

$$K_{11} = k_1 + k_2 - \left(\frac{1}{2}m_1 + \sum_{i=2}^{4} m_i\right)gL_1,$$

$$K_{22} = k_2 + k_3 - \left(\frac{1}{2}m_2 + \sum_{i=3}^{4} m_i\right)gL_2,$$

$$K_{33} = k_3 + k_4 - \left(\frac{1}{2}m_3 + m_4\right)gL_3,$$

$$K_{44} = k_4 - \frac{1}{2}m_4gL_4.$$

Taking the damping of the structure into account, its dynamic equation can be written as follows:

$$\mathbf{M}\ddot{\theta} + \mathbf{C}\dot{\theta} + \mathbf{K}\theta + \mathbf{N}(\theta) = \mathbf{F}\ddot{x}_b, \tag{26}$$

where the damping ratio is $\mathbf{C} = 2\zeta\mathbf{M}\boldsymbol{\Phi}\boldsymbol{\Lambda}\boldsymbol{\Phi}^{-1}$, Φ is the modal matrix, and Λ is a diagonal matrix consisting of the natural frequencies. For equipment without a shock absorber, $\mathbf{N}(\theta)$ in the dynamic equation can be omitted.

3. Seismic Response Analysis

3.1. Ground Motion Input. The seismic wave data adopted were those for artificial wave proposed by the China Electric Power Research Institute. The artificial wave was fitted based on a seismic acceleration response spectrum with a characteristic period of 0.9 s, capable of enveloping the characteristic periods of Category I_0–III soil sites, making them suitable for seismic design and testing and for seismic performance evaluation of HV and UHV electrical equipment [25]. The artificial wave time history and the curve fitted to the artificial wave response spectrum and target spectrum at peak seismic acceleration of 1 g are illustrated in Figure 11.

3.2. Experimental Verification of the Theoretical Model. To ensure that the theoretical model is correct and rational, its results under typical working conditions were compared with results from shaking table testing under the same conditions. During the test, strain gauges were arranged at the root of the porcelain bushing of each lightning arrester element, and the strain converted into a stress response using the elastic modulus. Accelerometers were arranged at the upper flange of each bushing element to provide data-permitting analysis of the dynamics of the equipment. The main operating condition applied during the test was white noise. The frequency of the equipment was tested under this condition and then under 0.3 g seismic test condition and 0.5 g shock absorption test conditions. At the end of the test, the relevant data and signal processing methods in mathematics are used to analyze the test data [26–28].

The natural frequencies of the equipment's seismic model and the shock absorption model were estimated, via solution for the eigenvalues of their dynamic equations, at 2.39 Hz and 2.27 Hz, respectively. These values were similar to the experimental estimates of 2.17 Hz and 2.08 Hz, representing errors of 10.14% and 9.13%, respectively.

Figure 12 provides a comparison of estimates for stress at the bottom of the porcelain pillars derived via theoretical analysis and testing under 0.3 g seismic effects. The results of the theoretical calculation are basically consistent with the experimental results. The maximum stress on the equipment derived from experimental and theoretical analyses was 22.02 MPa and 20.30 MPa, respectively, representing a difference in maximum stress of only 9.04%, confirming the validity of the seismic model without shock absorbers.

Figure 13 provides a comparison of time history for stress at the bottom of the porcelain pillar with shock absorption under a 0.5 g seismic effect. Once again, the results of the theoretical calculation are basically consistent with the experimental results. Estimates of the maximum stress on the equipment under a 0.5 g seismic effect were 11.5 MPa and 10.3 MPa, derived from experimental and theoretical analysis, respectively, representing a difference of only 10.4%, confirming the validity of the model with shock absorption.

3.3. Component Response under Seismic Excitation. To study the influence of ground motion intensity on the shock absorption of a 1000 kV pillar-type porcelain lightning arrester, a comparison of this equipment's seismic responses without and with shock absorption was conducted under conditions of 0.1 g, 0.2 g, 0.3 g, 0.4 g, and 0.5 g ground motion excitation. Figure 14 shows the stress response time history of the equipment for different magnitudes of ground motion excitation. The curve in Figure 15 describes the relationship between the magnitude of seismic wave excitation and shock absorption efficiency. Figure 16 shows the force-displacement relationships of a typical shock absorber under seismic effects of different magnitudes.

The results of this analysis show that as the intensity of seismic excitation increases, the loop in the hysteretic curve formed by the shock absorber increases in size, indicating that it dissipates more energy and has a larger effect, under increased seismic excitation. With seismic excitation of 0.1 g, 0.2 g, 0.3 g, 0.4 g, and 0.5 g, corresponding levels of shock absorption efficiency were 27.56%, 47.21%, 62.23%, 71.59%, and 77.49%, respectively. Absorption efficiency can be written as follows:

$$\eta = \frac{\sigma_1 - \sigma_2}{\sigma_1} \times 100\%, \tag{27}$$

where η is the absorption efficiency and σ_1 and $\sigma_2$are the stress on equipment under seismic conditions before and after installation of shock absorbers.

3.4. Influence of Shock Absorber Parameters on Equipment Seismic Response. Due to requirements concerning the stiffness characteristics of shock absorbers to be connected with electrical components during engineering application, in practice, the stiffness of different types of shock absorbers differs only slightly. Of all the shock absorber parameters, yield force is the main factor affecting their energy dissipation properties. The shock absorber installation radius—the radius of the circle around which the bolt holes for shock absorber installation are arranged—is also a key factor affecting their displacement energy dissipation properties. This study therefore focuses on the influence of shock absorbers' installation radius and yield force on their shock absorption efficiency.

To analyze the influence of the shock absorber installation radius on shock absorption efficiency, this parameter was varied over a 0.4–0.8 m range, and its influence on the shock absorption efficiency of the porcelain pillar system was examined for levels of seismic wave excitation intensity between 0.1 g and 0.5 g. Figure 17 depicts analytically derived relationships between shock absorber installation radius and the shock absorption efficiency of the pillar-type porcelain component. Table 2 shows how shock absorption efficiency varies with installation radius under different magnitudes of seismic excitation.

Figure 17 shows that for a given level of seismic wave excitation, shock absorption efficiency decreases gradually as shock absorber installation radius increases. Under seismic excitation of 0.5 g, shock absorption efficiency decreases from 81.51% to 62.20% as shock absorber installation radius

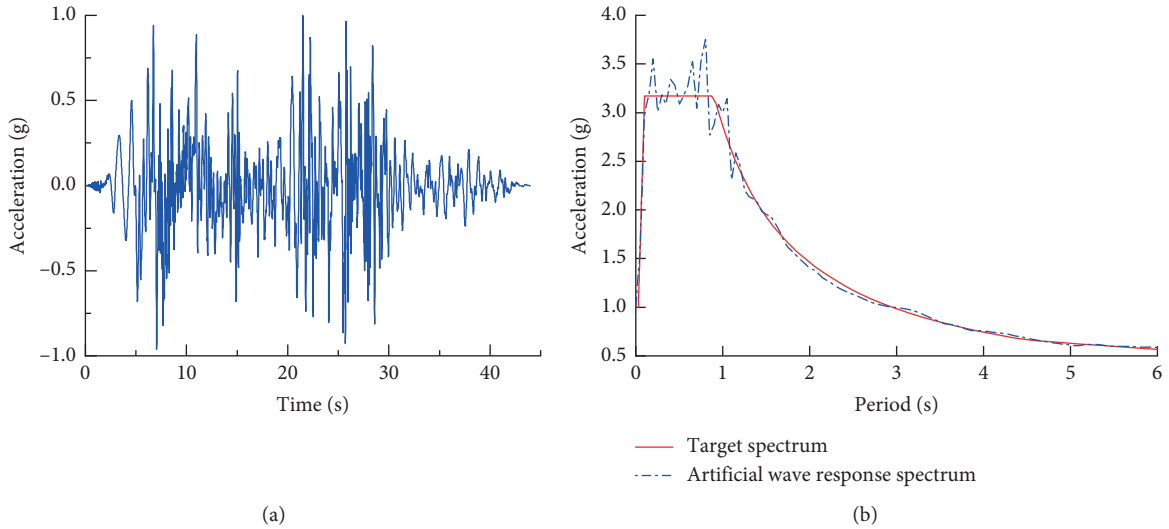

Figure 11: (a) Time history curve of artificial seismic wave. (b) Response-spectrum fitted curve.

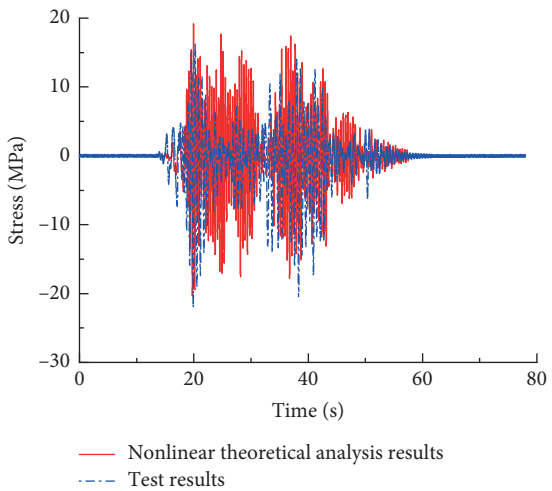

Figure 12: Stress at the bottom of the porcelain pillar under 0.3 g seismic effect.

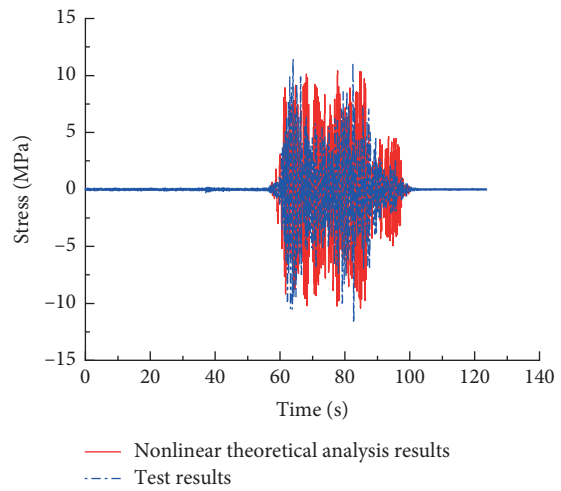

Figure 13: Stress at the bottom of the porcelain pillar under 0.5 g seismic effect with shock absorption.

increases from 0.4 m to 0.8 m. For lower magnitudes of seismic excitation, the porcelain pillar's shock absorption efficiency decreases more rapidly with increases in shock absorber installation radius: with seismic excitation of 0.1 g and a shock absorber installation radius of 0.8 m, shock absorption efficiency falls to the very low level of 3.94%. This represents a roughly 92% decrease in shock absorption efficiency compared with a shock absorber installation radius of 0.4 m. As seismic excitation gradually increases, the influence of shock absorber installation radius on the shock absorption efficiency of the porcelain pillar assembly gradually decreases. With 0.3 g seismic excitation and a 0.8 m installation radius, shock absorption efficiency is 38.74%, 45% lower than when the installation radius is 0.4 m. With 0.5 g seismic excitation and a 0.8 m installation radius, the shock absorption efficiency is 62.2%, only 24% lower than for 0.4 m installation radius. The degree to which shock absorption efficiency declines with installation radius gradually decreases as seismic excitation increases.

The influence of the shock absorber's yield force on shock absorption efficiency was analyzed by estimating the effect of parameter γ on shock absorption efficiency under different intensities of seismic excitation. Figure 18 shows how shock absorption efficiency changes with γ under different intensities of seismic excitation. Table 3 provides shock absorption efficiency values with different values of γ and seismic excitation. In the Bouc–Wen model, γ is closely related to the shock absorber's yield force, and the yield force values corresponding to the relevant values of γ are shown in Table 4.

As can be seen from Figure 18 and Table 3, for a given level of seismic excitation, shock absorption efficiency gradually increases as γ increases. With 0.1 g seismic excitation, shock absorption efficiency is 19.18% for $\gamma = 3{,}000$, rising to 27.56% for $\gamma = 7{,}000$, a 44% increase. With 0.3 g

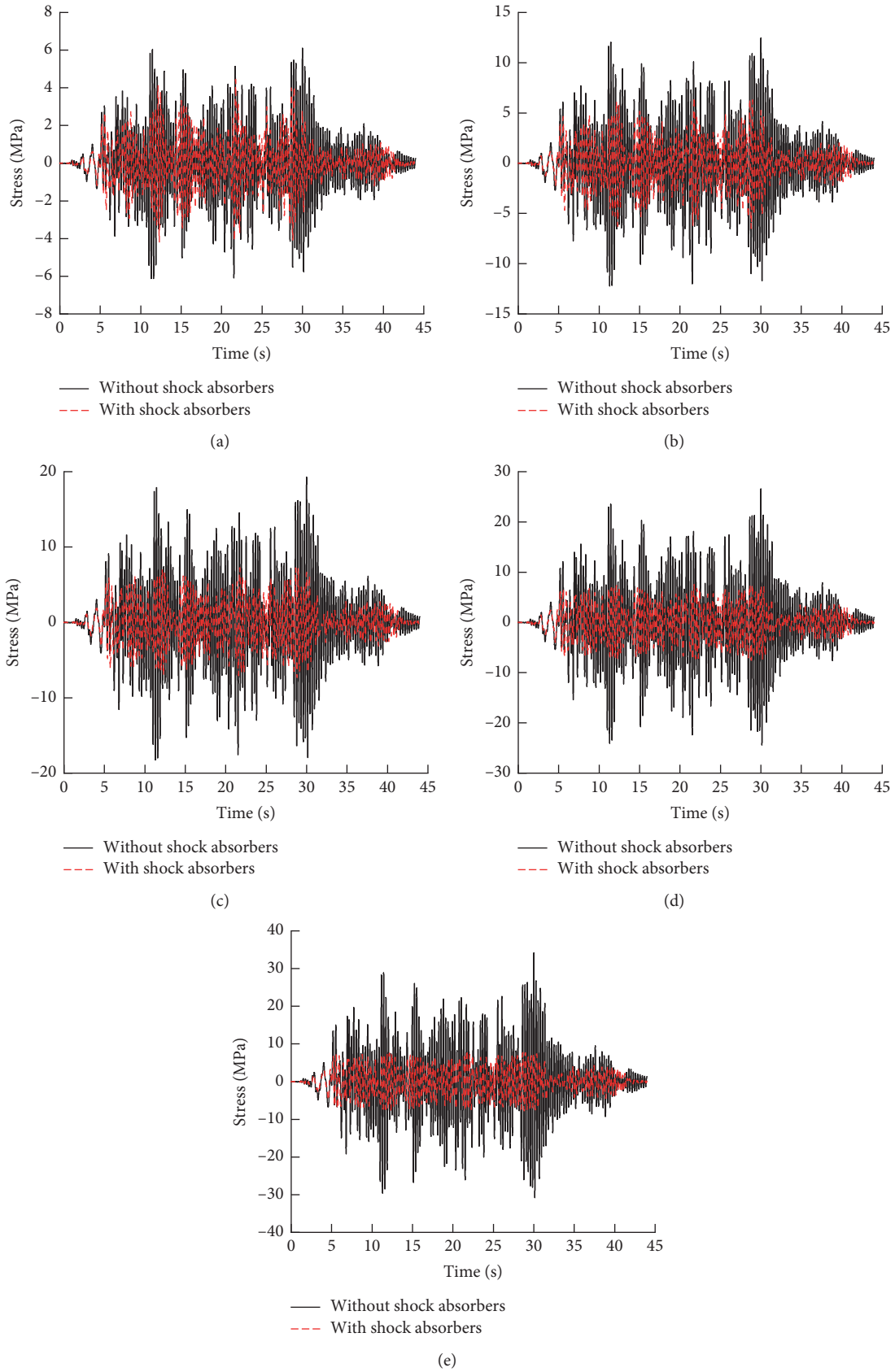

Figure 14: Stress at the bottom of the porcelain pillar under seismic excitation of different magnitudes: (a) 0.1 g, (b) 0.2 g, (c) 0.3 g, (d) 0.4 g, and (e) 0.5 g.

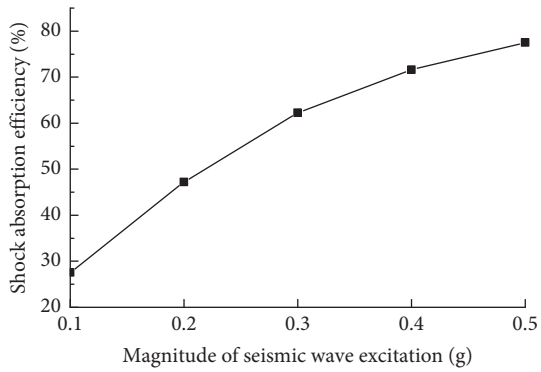

Figure 15: Relationship between seismic wave excitation and shock absorption efficiency.

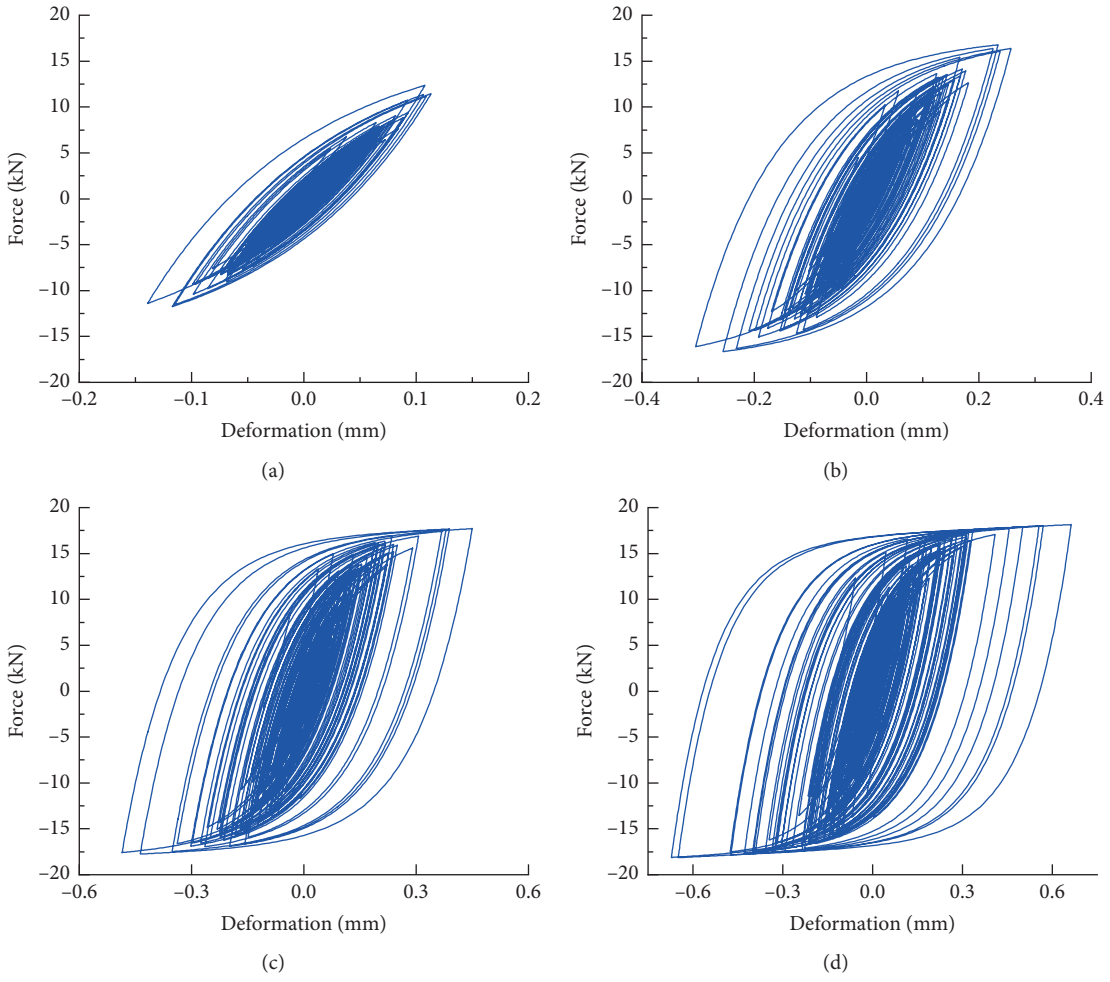

Figure 16: Continued.

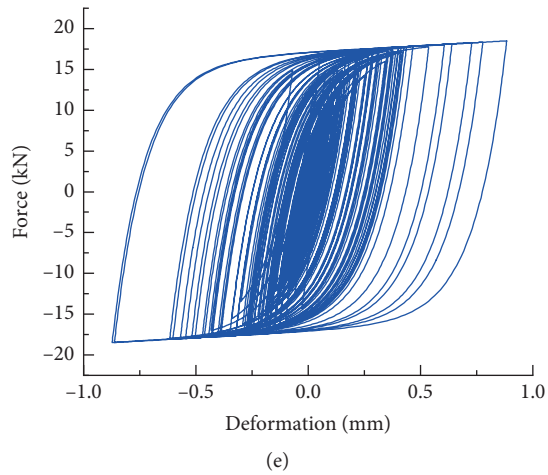

Figure 16: Force-displacement relationship of typical shock absorbers under seismic effects of different magnitudes: (a) 0.1 g, (b) 0.2 g, (c) 0.3 g, (d) 0.4 g, and (e) 0.5 g.

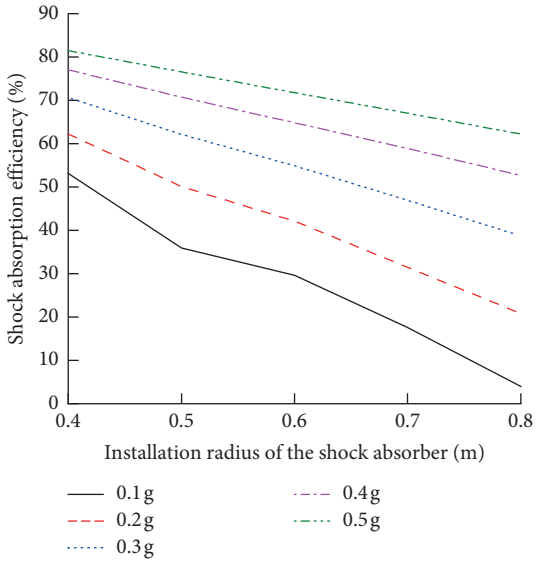

Figure 17: Influence of installation radius on porcelain pillar shock absorption efficiency.

Table 2: Shock absorption efficiency with different installation radii and magnitudes of seismic excitation.

Seismic excitation (g)	Shock absorption efficiency (%)		
	$R = 0.4$	$R = 0.6$	$R = 0.8$
0.1	53.11	29.62	3.94
0.2	62.2	42.14	20.85
0.3	70.67	54.86	38.74
0.4	77.05	64.85	52.67
0.5	81.51	71.80	62.20

seismic excitation, shock absorption efficiency is 35.97% for $\gamma = 3{,}000$, rising to 62.24% for $\gamma = 7{,}000$, a 73% increase. With 0.5 g seismic excitation, shock absorption efficiency is 53.86% for $\gamma = 3{,}000$, rising to 76.9% for $\gamma = 7{,}000$, a 43% increase.

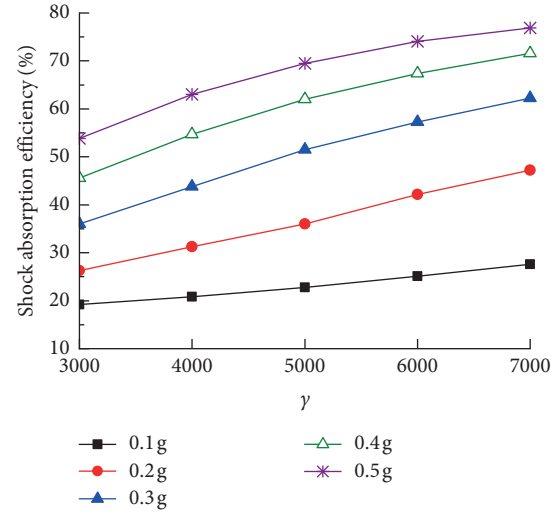

Figure 18: Relationship between shock absorption efficiency and γ.

Table 3: Shock absorption efficiency with different values of γ and magnitudes of seismic excitation.

Seismic excitation (g)	Shock absorption efficiency (%)				
	$\gamma = 3000$	$\gamma = 4000$	$\gamma = 5000$	$\gamma = 6000$	$\gamma = 7000$
0.1	19.18	20.81	22.80	25.07	27.56
0.2	26.29	31.29	36.00	42.12	47.21
0.3	35.97	43.80	51.50	57.25	62.24
0.4	45.60	54.71	62.00	67.42	71.60
0.5	53.86	63.02	69.47	74.07	76.90

Table 4: Yield force of shock absorber for different values of γ.

γ Value	3000	4000	5000	6000	7000
Yield force (kN)	40	30	25	20	18

For a given value of γ, shock absorption efficiency gradually increases with seismic excitation. For $\gamma = 3{,}000$, shock absorption efficiency is 53.86% for 0.5 g seismic

excitation, representing a significant increase of 180% compared to efficiency with 0.1 g seismic excitation. For $\gamma = 5{,}000$, shock absorption efficiency under 0.5 g seismic excitation is 204% higher than that under 0.1 g seismic excitation. For $\gamma = 7{,}000$, shock absorption efficiency under 0.5 g seismic excitation is 179% higher than that under 0.1 g seismic excitation.

These estimates show that for a given level of seismic excitation, the smaller the shock absorber's yield force, the higher the shock absorption efficiency; with the decrease of yield force, the increasing amplitude of shock absorption efficiency increases first and then decreases.

4. Conclusions

This paper applies the Bouc–Wen model to fit restoring force-displacement curves for hysteretic nonlinear metal shock absorbers, avoiding the sharp inflection points introduced by bilinear models. Dynamic models and equations for pillar-type porcelain electrical components were developed, taking their nonlinear characteristics into consideration, allowing examination of the effects of shock absorbers on these components' nonlinear seismic responses. This yielded the following conclusions:

(1) Shaking table test results indicated small differences, not exceeding 11%, between the theoretically and experimentally derived results, illustrating the accuracy of the theoretical model and results derived from this theoretical analysis. This validates the correctness and reasonableness of results from the theoretical model.

(2) Under seismic wave excitation, porcelain pillars' vibration responses can be effectively suppressed using hysteretic nonlinear shock absorbers. The greater the seismic wave intensity, shock absorption devices enter the yield state better and absorb more seismic energy, and thus, the more obvious the efficiency of this shock absorption.

(3) As the installation radius and yield force of the shock absorber increase, its shock absorption efficiency gradually decreases. Thus, during engineering design, reasonable values for the yield force and installation radius of shock absorbers should be selected based on structural characteristics and the required degrees of seismic fortification and the required shock absorption efficiency of the equipment.

(4) For the shock absorption design of electrical equipment in high seismic intensity area, shock absorption efficiency should be more than 50%. During the shock absorption design of 1000 kV arrester equipment, to ensure perfect absorption efficiency under 0.4 g earthquake, the yield force should be between 18 kN~30 kN, and the installation radius of shock absorbers should be about 0.6 m.

Data Availability

The data used to derive the findings of this study are available from the corresponding author upon request.

Conflicts of Interest

The authors declare that there are no conflicts of interest regarding the publication of this paper.

Acknowledgments

This study was funded by the Chinese National Key R&D Program (2018YFC0809400).

References

[1] Y. Yu, G. Li, L. Peng et al., "Investigation and analysis of electric equipment damage in Sichuan power grid caused by Wenchuan earthquake," *Power System Technology*, vol. 32, no. 11, pp. 1–6, 2008.

[2] N. Qiu, Y. Cheng, M. Zhong, Z. Lu, Z. Zhu, and X. Lu, "Progress and prospects in seismic research of 1000 kV UHV AC electrical equipment," *High Voltage Engineering*, vol. 41, no. 5, pp. 1732–1739, 2015.

[3] Y. Cheng, Z. Quanjun, and Z. Lu, "Progress and development trends on seismic measures of electric power equipments in transformer substation," *Power System Technology*, vol. 32, no. 22, pp. 84–89, 2008.

[4] J. Anshel and K. Leon, "IEEE 693 Seismic qualification of composite for substation high-voltage equipment," in *Proceedins of the 13th World Conference on Earthquake Engineering*, Vancouver, Canada, August 2004.

[5] L. Zhenlin, D. Zebing, and L. Zhicheng, "Weibull distribution based seismic vulnerability analysis of porcelain power equipment," *Power System Technology*, vol. 38, no. 4, pp. 1076–1081, 2014.

[6] J. Song, A. Der Kiureghian, and J. L. Sackman, "Seismic interaction in electrical substation equipment connected by non-linear rigid bus conductors," *Earthquake Engineering & Structural Dynamics*, vol. 36, no. 2, pp. 167–190, 2010.

[7] J.-P. Dastous and J.-H. Pierre, "Experimental investigation on the dynamic behavior of flexible conductors between substation equipment during an earthquake," *IEEE Transactions on Power Delivery*, vol. 11, no. 2, pp. 801–807, 1996.

[8] H. Ghalibafian, G. S. Bhuyan, C. Ventura et al., "Seismic behavior of flexible conductors connecting substation equipment-part II: shake table tests," *IEEE Transactions on Power Delivery*, vol. 19, no. 4, pp. 1680–1687, 2004.

[9] A. D. Kiureghian, J. L. Sackman, and K. J. Hong, *Interaction in Interconnected Electrical Substation Equipment Subjected to Earthquake Ground motions*, Pacific Earthquake Engineering Research Center, Richmond, CA, USA, 1999.

[10] A. D. Kiureghian, K. J. Hong, and J. L. Sackman, *Further Studies on Seismic Interaction in Interacted Electrical Substation equipment*, Pacific Earthquake Engineering Research Center, Richmond, CA, USA, 2000.

[11] F. Paolacci, R. Giannini, S. Alessandri, and G. De Felice, "Seismic vulnerability assessment of a high voltage disconnect switch," *Soil Dynamics and Earthquake Engineering*, vol. 67, pp. 198–207, 2014.

[12] R. Karami Mohammadi and A. Pourkashani Tehrani, "An investigation on seismic behavior of three interconnected pieces of substation equipment," *IEEE Transactions on Power Delivery*, vol. 29, no. 4, pp. 1613–1620, 2014.

[13] R. K. Mohammadi, F. Nikfar, and V. Akrami, "Estimation of required slack for conductors connecting substation equipment subjected to earthquake," *IEEE Transactions on Power Delivery*, vol. 27, no. 2, pp. 709–717, 2012.

[14] A. Filiatrault and C. Stearns, "An experimental study on the seismic response of electrical substation equipment interconnected by flexible conductors," in *Proceedings of the Advancing Mitigation Technologies & Disaster Response for Lifeline Systems*, pp. 667–676, Long Beach, CA, USA, August 2003.

[15] K. M. Mosalam and S. Günay, "Seismic performance evaluation of high voltage disconnect switches using real-time hybrid simulation: I. System development and validation," *Earthquake Engineering & Structural Dynamics*, vol. 43, no. 8, pp. 1205–1222, 2014.

[16] Y.-F. Cheng, Z.-B. Dai, L. U. Zhi-Cheng et al., "Study on method of seismic design for electrical equipment with engrgy dissipation devices in China," *High Voltage Apparatus*, vol. 49, no. 9, pp. 69–79, 2013.

[17] Y. Cheng, H. Guo, Z. Zhu, X. Su, and Y. Chen, "Dynamics of a upright Pole coupled with nonlinear hysteretic isolators under harmonic base excitation," *Shock and Vibration*, vol. 2018, Article ID 2497035, 11 pages, 2018.

[18] Y. Cheng, X. Meng, Z. Lu, Z. Liu, N. Qiu, and Y. Ma, "Shaking table test on the seismic performance of ultrahigh voltage interconnected electrical equipment," *China Earthquake Engineering Journal*, vol. 42, no. 2, pp. 292–298, 2019.

[19] L. Ye, X. Lu, Q. Ma, X. Wang, and Z. Miao, "Nonlinear analytical models, methods and examples for concrete structures subject to earthquake loading," *Engineering Mechanics*, vol. 23, no. Sup.2, pp. 131–141, 2006.

[20] J.-B. Dastous and J.-Y. Paquin, "Testing and development of alternative flexible-bus geometries for interconnected substation equipment subjected to earthquakes," *IEEE Transactions on Power Delivery*, vol. 18, no. 3, pp. 772–780, 2003.

[21] J.-B. Dastous, "Guidelines for seismic design of flexible buswork between substation equipmenf," *Earthquake Engineering and Structural Dynamics*, vol. 36, no. 8, pp. 191–208, 2007.

[22] J.-B. Dastous and J.-R. Pierre, "Design methodology for flexible buswork between substation equipment subjected to earthquakes," *IEEE Transactions on Power Delivery*, vol. 22, no. 3, pp. 1490–1497, 2007.

[23] R. M. Mutobe and T. R. Cooper, "Nonlinear analysis of a large bridge with isolation bearings," *Computers & Structures*, vol. 72, no. 1–3, pp. 279–292, 1999.

[24] Q/GDW 11132-2013, *Technical Specification for Seismic Design of Ultra-high Voltage Porcelain Insulating Equipments and Installation/Maintenance to Energy Dissipation Devices*, China Electric Power Press, Beijing, China, 2014.

[25] Z. Liu, Y. Cheng, Z. Lu et al., "Shake table test on UHV standardization lightning arrester installed with shear-type lead dampers," *High Voltage Engineering*, vol. 44, no. 8, pp. 2595–2602, 2018.

[26] D. Zhao, S. X. Ding, H. R. Karimi, and Y. Li, "Robust $H_ \infty$ filtering for two-dimensional uncertain linear discrete time-varying systems: a krein space-based method," *IEEE Transactions on Automatic Control*, vol. 64, no. 12, pp. 5124–5131, 2019.

[27] D. Zhao, Y. Li, C. Ki Ahn, and S. X. Ding, "Optimal state and fault estimation for two-dimensional discrete systems," *Automatica*, vol. 115, p. 108856, 2020.

[28] Z. Dong, H. K. Lam, Y. Li, S. X. Ding, and S. Liu, "A novel approach to state and unknown input estimation for Takagi-Sugeno fuzzy models with applications to fault detection," *IEEE Transactions on Circuits and Systems I: Regular Papers*, pp. 1–11, 2020.